Ocean Science

Retroflection from slanted coastlines-circumventing the "vorticity paradox"

V. Zharkov[1] and D. Nof[1,2]

[1]Geophysical Fluid Dynamics institute, Florida State University, USA
[2]Department of Oceanography, Florida State University, USA

Abstract. The balance of long-shore momentum flux requires that the solution of *zonally* retroflecting currents involve ring shedding on the western side. An important aspect of the ring dynamics is the ring intensity α (analogous to the Rossby number), which reaches its maximum value of unity when the upstream potential vorticity (PV) is zero. Friction leads to a slow-down and a decrease in α. The main difficulty is that the solution of the system of equations for conservation of mass and momentum of *zonal* currents leads to the conclusion that the ratio (Φ) of the mass flux going into the rings and the total incoming mass flux is approximately $4\alpha/(1+2\alpha)$. This yields the "vorticity paradox" – only relatively weak rings ($\alpha \leq 1/2$) could satisfy the necessary condition $\Phi \leq 1$. Physically, this means, for example, that the momentum-flux of zero PV currents upstream is so high that, no matter how many rings are produced and, no matter what size they are, they cannot compensate for it.

To avoid this paradox, we develop a nonlinear analytical model of retroflection from a slanted *non-zonal* coastline. We show that when the slant of coastline (γ) exceeds merely 15^0, Φ does not reach unity *regardless* of the value of α. Namely, the paradox disappears even for small slants. Our slowly varying nonlinear solution does not only let us circumvent the paradox. It also gives a detailed description of the rings growth rate and the mass flux going into the rings as a function of time. For example, in the case of zero PV and zero thickness of the upper layer along the coastline, the maximal values of Φ can be approximately expressed as, $1.012+0.32\exp(-\gamma/3.41)-\gamma/225$. Interestingly, for significant slants ($\gamma \geq 30^0$), the rings reach a *terminal size* corresponding to a balance between the β-force and both the upstream and downstream momentum fluxes. This terminal size is unrelated to the ultimate detachment and westward drift due to β. Our analytical solutions are in satisfactory agreement with the results of a numerical model that we run.

1 Introduction

Recent hypotheses regarding retroflecting currents, such as the North Brazil Current, the Agulhas Current (AC), and the East Australian Current, have put forward the idea that rings are shed primarily by inertial and momentum imbalances, rather than by local instabilities, upstream variability or coastline curvature. For example, regarding the AC (whose rings play a very important role in the exchange between the Indian and the Atlantic Oceans), this suggestion is supported by observations that the Agulhas eddies correspond to a primarily zonal protrusion of the parent current and are typically larger than rings produced by instability. Ou and De Ruijter (1986) argued that the curvature of the South American coast forces the coast to "separate from the AC" rather than the AC to separate from the coast. Under such conditions, inertia forces the current to make a loop that closes upon itself, forming a ring. Nof and Pichevin (1996), and Pichevin et al. (1999) proposed a purely inertial mechanism of ring formation, in the context of a reduced gravity model in which the retroflection of a *zonally* flowing current is "prescribed" through inflow conditions. It was shown that taking into account the development of eddies on the western side allows one to balance the alongshore momentum flux, that is, to resolve the so-called "retroflection paradox". The theoretically obtained periods of eddy formation were shown to be roughly in accordance with the observations, although the obtained radii were about twice as large as typical observed values. As an integrated constraint, the solution did
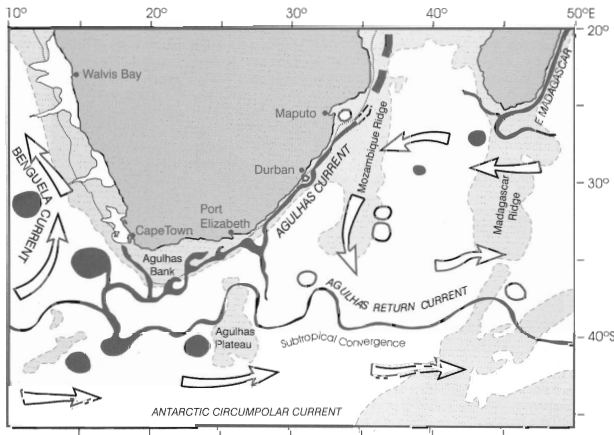
Fig. 1. A conceptual portrayal of the AC system. Areas shallower than 3000 m are shaded. The edge of the continental shelf is represented by the dotted line at the 500 m isobath. Intense currents and their component parts are black; the general background circulation is indicated by open arrow. Cyclonic eddies are open; anti-cyclonic rings and eddies black. Adapted from Lutjeharms (2006).

not allow for detailed calculations of many details such as the rings' growth rate. These detailed calculations, which were not done in the earlier studies, are the focus of the present work.

Observations suggest that the rings mass transport into the Southern Atlantic is about 3–20% of the total mass flux of the AC (Lutjeharms, 2006). Using the slowly varying approach, we will show here (analytically and numerically) that the approximation of a purely *zonal* retroflection (Nof and Pichevin, 1996) leads to the conclusion that only weak eddies (i.e., whose vorticity is small) can be formed. We will refer to this peculiar aspect as the "*vorticity paradox*".

We shall show that one way to circumvent this paradox is to consider *slanted* coastlines instead of *zonal* ones. This does not really *resolve* the paradox but it does take us away from it allowing us to derive a detailed solution. Accordingly, we shall focus on the role that the *angle* of the coastal slant plays in the AC retroflection. Our solution will show that an increased slant of the coastline leads to a decrease in the mass flux going into the rings. In the limit of a meridional boundary (90° slant), no eddies are formed.

1.1 Observational background

The AC, whose estimated transport is about 65–70 Sv (Gordon et al., 1987), is presently the strongest western boundary current (WBC) in the world ocean (Fig. 1). It is an important part of the subtropical "super gyre" whose southern boundary is largely determined by the position of the zero wind stress curl (de Ruijter, 1982). The rings shed from the AC are responsible for transporting most of the water masses from the Indian Ocean into the South Atlantic and, therefore, con-

tribute to the near-surface return flow of the North Atlantic Deep Water (NADW) from the Pacific and Indian Oceans to the North Atlantic. The annual transport (into the South Atlantic) associated with an average Agulhas ring is estimated to be between 0.4 and 3.0 Sv (de Ruijter et al., 1999), with correspondingly large ranges in the heat and salt anomaly estimates. Estimates of the rings' radius vary. For example, while direct observations suggest that "Astrid" was 140 km in radius (van Aken et al., 2003), the METEOSAT satellite data points to 162 km (Lutjeharms, 2006). Since there are several rings shed every year, their common transport is 3–10 Sv representing a significant part of the meridional overturning circulation (MOC). Weijer et al. (1999) showed that the saline source of Agulhas water stabilizes the MOC whereas the fresher cold-water flux from the Arctic Ocean destabilizes it.

1.2 Theoretical background

The retroflection process in question involves two different aspects. First, within the context of a 1.5-layer model, Nof and Pichevin (1996) showed that, in the case of a nearly *zonal* coastline, westward-drifting rings must be generated to resolve the so-called "retroflection paradox". On the other hand, in the case of exactly *meridionally* directed incident current, *no* eddy detachment has been exhibited in both analytical and numerical models (Arruda et al., 2004). Namely, if the ratio of mass flux going into the eddies and incoming flux is denoted by $\Phi = (Q-q)/Q$ (where Q and q are the mass fluxes of incoming and retroflected currents), then Φ is maximal in the case of a *zonal* boundary and zero in the case of a strictly *meridional* boundary. Therefore, Φ is expected to be monotonically decreasing as a function of the coastline slant, γ.

The second important aspect is the eddy radius (R). For the related case of ballooning outflows (i.e., outflows from a narrow channel on an f plane), Nof and Pichevin (2001, NP, hereafter) and Nof (2005) showed that the basic eddy (i.e., the eddy next to the channel mouth, hereafter referred to as BE) radius increases with time as $t^{1/4}$. A similar behavior is to be expected in our present case of currents retroflecting from *zonal* coasts. However, as mentioned, when the coastline is nearly *meridional*, Φ is nearly zero so that the eddy growth rate is nearly zero. Consequently, the final radius, R_f, is expected to decrease as the slant increases.

The effect of a coastal slant on these aspects is, evidently, essential. Some of this was recognized before – the importance of coastal geometry was mentioned by Ou and de Ruijter (1986), Boudra and Chassignet (1988), Chassignet and Boudra (1988), de Ruijter et al. (1999), and Pichevin et al. (1999). However, none of the above points to the issues that we are addressing here, the significance of the AC intensity, and the issue of eddy generation.

1.3 Present approach

As mentioned, we will develop a nonlinear retroflection model (Fig. 2) using the slowly varying approach suggested by Nof (2005) and will include a nonzero slant (γ) and a finite thickness of the upper layer surrounding the retroflection (H). We shall consider here the development of the BE before its detachment, which is due to the β-induced westward movement. We will show that an increased slant of the coastline slows down the rings' growth rate and leads to a rapid decrease in Φ. As mentioned, this will enable us to avoid the "vorticity paradox".

The paper is organized as follows. In Sect. 2, we will discuss the "vorticity paradox" in relation to the retroflection from *zonal* coastline, and then deduce the governing equations that control the development of BE in the case of retroflection from a *slanted* coastline. In Sect. 3, we derive the analytical expressions for all the terms in these equations and in Sect. 4, we will present the numerical resolutions. Section 5 is devoted to comparisons of our results with numerical simulations, and Sect. 6 summarizes our results.

2 Statement of problem

This section contains the physics of the problem and the mathematical approach. Following Pichevin et al. (1999), we consider a boundary current (with density ρ) embedded in an infinitely deep, stagnant lower layer with density ($\rho + \Delta \rho$). The current is flowing along a rectilinear wall and retroflects (Fig. 2). The cause of the retroflection is not important for our consideration but one may assume that it is due to a vanishing wind stress curl. The wall is not *zonal* – the *slant* (γ) varies between zero for a zonal coastline and 90^0 for a meridional coastline.

Following NP, we will use an expansion in $\varepsilon = (\beta R_d / f_0) \sim O(0.01)$, where R_d is the Rossby radius and f_0 the mean absolute value of Coriolis parameter. (All of our variables are conventionally defined in both the text and Appendix A.) The small parameter ε represents the relation between the scale of the eddy and the Earth's radius. We shall consider either a BE whose PV was nonzero to begin with, or an eddy whose PV has been gradually altered by frictional processes over a very long period. We shall suppose that the BE main orbital flow ($\overline{v_\theta}$) is,

$$\overline{v_\theta} = -\frac{\alpha f r}{2}, \alpha \le 1, \tag{1}$$

where f, the Coriolis parameter, is nearly constant at the scale of the eddy, α measures the eddy intensity (and is twice the familiar Rossby number), and the bar indicates that we speak about the basic f-plane state. Note that, for an incoming flow emptying into the ocean through a narrow channel, NP showed that $\Phi = 2\alpha/(2\alpha + 1)$. In that case, there is no "vorticity paradox" because Φ is smaller than unity for all
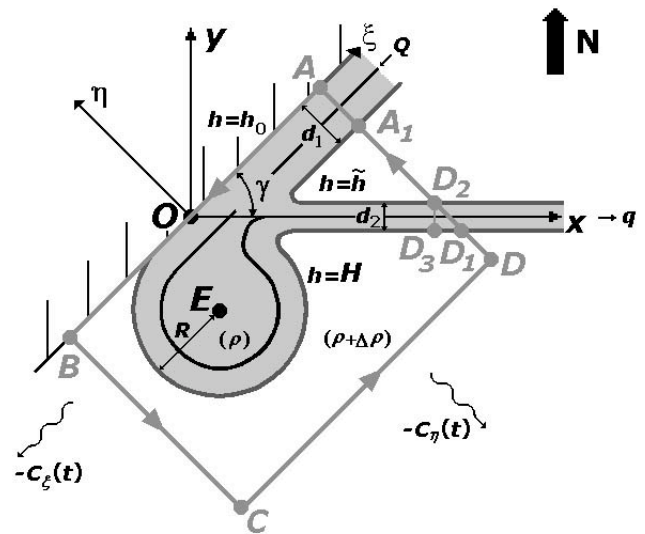

Fig. 2. A schematic diagram of the model under study. E is the center of the BE. In the (rotated) coordinate system ξ is directed along the coastline, and η is directed normal to the coastline. The incoming flux Q flows along the wall whereas the outgoing (retroflected) flux q is directed to the east. The widths of the currents are d_1 and d_2, respectively. The "wiggly" arrow indicates the migration of the BE; it results from both the eddy growth, which forces the eddy away from the wall, and from β, which forces the eddy along the wall. We shall see that the migration $C_\eta(t)$ is primarily due to the growth, whereas $C_\xi(t)$ is primarily due to β. The thick grey line (with arrows) indicates the integration path, $ABCDA$; $\widetilde{h}$ is the upper layer thickness of the stagnant region wedged in between the upstream and retroflecting current, and H is the off-shore thickness. The segment $D_2 D_3$ is involved in the expressions containing γ.

α. This is because, in the NP outflow problem, the momentum of only *one* current needs to be compensated for by the rings whereas *two* currents need to be compensated for in the retroflection case discussed here.

Following the NP approach (see their (3.2b) where $R_d = 2^{-3/2} R$), we find that the volume conservation for a retroflecting current is,

$$Q - q = \frac{dV}{dt} = \frac{\pi \alpha (2 - \alpha) f^2 R^3}{4g'} \frac{dR}{dt}, \tag{2}$$

where g' is the reduced gravity, and $R(t)$ is the radius of BE. Similarly, the momentum-flux balance for a *zonal* retroflecting current yields (instead of (3.3b) in NP),

$$-\frac{\alpha f R(Q + q)}{2} + C_y \iint\limits_s f \overline{h} dx dy = 0. \tag{3}$$

The first term is the momentum flux of the upstream and retroflecting current whereas the second is the integrated Coriolis force associated with the movement of the eddy off

the wall. As in NP, we assume that $C_y = dR/dt$ and get a second equation for Q and q,

$$Q + q = \frac{\pi(2-\alpha)f^2 R^3}{8g'}\frac{dR}{dt},\tag{4}$$

which, with Eq. (2), gives,

$$\Phi = \frac{4\alpha}{1+2\alpha}.\tag{5}$$

Recall that, according to mass conservation, Φ is a ratio of the mass flux going into eddies and the total incoming mass flux, so it cannot exceed unity. This introduces the "vorticity paradox" – the problem has a *physically meaningful* solution only in the case of weak eddies when $\alpha \leq 1/2$. This is because, in the strong inertial limit (α larger than $1/2$), the momentum flux of the retroflecting current is just too high for rings to compensate for it, no matter how many rings there are and, no matter how large they are.

We shall circumvent this paradox by varying the thickness of the upper water near the wall (h_0), the off-shore thickness outside the retroflection region (H), α, and γ. We will use an off-shore and a long-shore coordinate system (ξ, η) moving with the BE (Fig. 2) involving the familiar transformation formulae, $\xi = x\cos\gamma + y\sin\gamma$, $\eta = -x\sin\gamma + y\cos\gamma$.

2.1 Conservation of volume

The integrated volume conservation equation is,

$$\frac{d}{dt}\iint_s h\,d\xi\,d\eta = Q - q.\tag{6}$$

Recall that the relationships between our moving coordinates ξ and η, time t, and $\hat{\xi}$, $\hat{\eta}$, $\hat{t}$ in the fixed system are: $\xi = \hat{\xi} - \int_0^{\hat{t}} C_\xi dt$, $\eta = \hat{\eta} - \int_0^{\hat{t}} C_\eta dt$, and $\hat{t} = t$. Following NP, we will assume that the shape of the BE is nearly circular. We will see (from our numerical simulations) that this approximation is satisfied for the mean, but not for very small α because, in this limit, the BE is very large. Our next important point concerns the magnitude of q. In the earlier studies, Φ was found to be nearly constant. In contrast, we will show here that q, and therefore Φ, will vary dramatically in time, implying that the differential equations describing the growth of the BE are strongly non-linear.

2.2 Momentum flux

We first introduce the stream-function ψ, defined by $\partial\psi/\partial\eta = -h\boldsymbol{u}^* \partial\psi/\partial\xi = hv^*$. This is allowable because, with our slowly varying approximation, the vector field $h\boldsymbol{u}^*$ is approximately non-divergent. Using the continuity equation, we write the momentum equations in the form:

$$-\frac{\partial^2\psi}{\partial\eta\partial t} + h\frac{\partial C_\xi}{\partial t} + \frac{\partial(h\boldsymbol{u}^{*2})}{\partial\xi} + \frac{\partial(h\boldsymbol{u}^*v^*)}{\partial\eta} - f\frac{\partial\psi}{\partial\xi}$$
$$-fhC_\eta + \frac{g'}{2}\frac{\partial h^2}{\partial\xi} = 0,\tag{7a}$$

$$\frac{\partial^2\psi}{\partial\xi\partial t} + h\frac{\partial C_\eta}{\partial t} + \frac{\partial(h\boldsymbol{u}^*v^*)}{\partial\xi} + \frac{\partial(hv^{*2})}{\partial\eta} - f\frac{\partial\psi}{\partial\eta}$$
$$+fhC_\xi + \frac{g'}{2}\frac{\partial h^2}{\partial\eta} = 0.\tag{7b}$$

Here, $f = -f_0 + \beta\xi\sin\gamma$, where f_0 is positive for the Southern Hemisphere. The stars indicate that the variable in question is in the new, moving coordinate system. As in NP, Eq. (7b) cannot be used because, with our approach, it is impossible to calculate the pressure exerted by the wall on the BE.

Next, Eq. (7a) is integrated over the area bounded by the thick grey arrowed line shown in Fig. 2. Using Stokes' theorem, and taking into account that $\partial f/\partial\xi = \beta\sin\gamma$, one obtains,

$$\oint_\phi \left[\frac{\partial\psi}{\partial t} - h\boldsymbol{u}^*v^*\right]d\xi + \oint_\phi \left[h\boldsymbol{u}^{*2} + \frac{g'h^2}{2} - f\psi\right]d\eta$$
$$+ \iint_s \left[h\frac{\partial C_\xi}{\partial t} - \beta|\psi|\sin\gamma - fhC_\eta\right]d\xi\,d\eta = 0.\tag{8}$$

Following NP, we now introduce a "fast" time scale, $\sim O(f_0^{-1})$, and a "slow" time scale, $\sim O(\beta R_d)^{-1}$. We will see that, such a definition of time scales, is valid not only when the BE is well developed but also at the beginning of the BE developmental stage. With the slowly varying approximation one neglects the time derivatives in the momentum equations upfront (i.e., the terms containing $\partial\psi/\partial t$ and $\partial C_\xi/\partial t$ in Eq. 8) but keeps the time dependent terms in the bulk continuity equation. We point out in passing that, because of the eddy is radially symmetric, the first time dependent term in Eq. (8) is negligible even without the slowly varying approximation.

Geostrophy of the one-dimensional upstream currents implies that we cannot take $h \equiv 0$ outside the retroflection region because, with zero thickness outside, there is no net volume flux going into the rings. Hence, the thickness off-shore will be taken to be H. The slowness of the BE generation process enables us to assume geostrophic balance along the downstream retroflected current. Nof and Pichevin (1996) showed that, in such a case, we may neglect the sum of the terms $g'h^2/2$ and $-f\psi$ (integrated over η) in Eq. (8), assuming ψ to be zero outside the BE. The term $-h\boldsymbol{u}^*v^*$ integrated over ξ is also negligible because $v^* \equiv 0$ along the wall, and disturbances outside the BE are small. Finally, the main contributions to the integral $\oint_\phi h\boldsymbol{u}^{*2}d\eta$ are $\int_A^{A_1} h\boldsymbol{u}^{*2}d(-\eta)$, from the

incoming current, and $\int\limits_{D_2}^{D_1} h u^{*2} d\,(-\eta)$, from the retroflected current. It is easy to demonstrate that the last term is equal to $\int\limits_{D_2}^{D_3} h u^{*2} d\,(-y) \times \cos\gamma$, where $D_3 D_2$ is shown in Fig. 2. In view of this, we re-write Eq. (8) in the form:

$$F_1 + F_2 \cos\gamma - F_3 - F_4 \sin\gamma = 0, \tag{9}$$

where $F_1 = \int\limits_{A}^{A_1} h u^{*2} dl$, $F_2 = \int\limits_{D_2}^{D_3} h u^{*2} dl$, $F_3 = C_\eta \iint\limits_s f h d\xi d\eta$, and $F_4 = \beta \int\int\limits_s |\psi| d\xi d\eta$.

Equation (9) represents a balance of four forces. The first term is the force (i.e., momentum-flux) produced by the incoming current flowing along the slanted coast. The second is the force of the zonally retroflected current downstream. The third is the integrated Coriolis force resulting from the growth of the BE which forces its center to migrate off-shore. Finally, the fourth is an equatorward β-force resulting from the counterclockwise rotation of eddy particles within the BE (in the Southern Hemisphere). We note that, in the third term, both C_η and f are negative; for the Northern Hemisphere, Eq. (9) remains the same, but with positive C_η and positive f. In the case $\gamma = 90^0$, Eq. (9) takes the form of the meridional momentum balance considered by Arruda et al. (2004). Because the BE can only touch the wall, we do not expect the so-called "image effect" to be important and neither do we expect leakages of the kind discussed by Nof (1999) to be important. Unfortunately, we know of no scaling that can support these choices and we will make these two assumptions with the understanding that the numerics will provide the test for their validity. We shall see that the neglect of these two processes is indeed justified.

3 Analytical approach

3.1 The "small distortion approximation"

We assume that our problem is slowly varying in time, and that the BE boundary is approximately circular. We note that the BE does not have to conserve PV on the long timescale, but must conserve it on the short timescale. Namely, at each moment of time, the PV of the BE must be equal to that of the retroflected current. However, the frictional effects can accumulate over the long time period to become significant and, hence, can alter the PV. We can re-write Eq. (6) in the form:

$$\frac{dV}{dt} = Q - q, \tag{10}$$

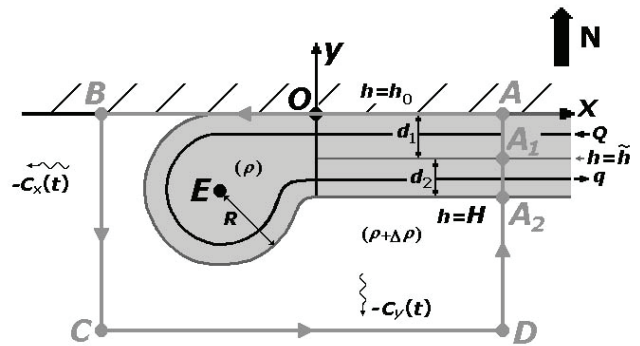where V is the BE volume (to be expressed as a function of its radius).

Fig. 3. A schematic diagram of the model in the special case of a *zonal* coastline. Here, we use the coordinate system (x, y). The fluxes Q and q are separated by the streamline at $x > 0$ and $y = -d_1$, so that the combined segment $A A_2$ serves as an analog of both $A A_1$ and $D_2 D_1$ shown in Fig. 2. The "wiggly" arrows show the migration of the eddy (southward on account of the BE growth, and westward due to β).

3.2 Properties of the $\gamma \to 0$ case

In this case, the incoming and retroflected currents are joined (in the sense that A_1 coincides with D_2), so that instead of having two segments we now have one combined $A D_3$. For convenience, we re-drew this special case (Fig. 3) introducing the new notations and returning to the original coordinate system (x, y). The integration segment for F_2 is now $A_1 A_2$ so that we have,

$$F_1 = \int\limits_0^{d_1} h u^2 d(-y),$$

$$F_2 = \int\limits_{d_1}^{d_1+d_2} h u^2 d(-y),$$

$$F_4 = \beta \iint\limits_s |\psi| dx dy, \tag{11}$$

where the expression for F_3 remains the same as before, and d_1 and d_2 are the widths of the incoming and retroflected currents.

We introduce the polar coordinate system (r, θ) centered at E and assume that Eq. (1) applies, where $f \approx -f_0$. We also require conservation of the Bernoulli integral along the outer edge of the retroflected current ($h = H$) and the BE so that one of our boundary conditions is,

$$u\,|_{y=-(d_1+d_2)} = u_1 = \frac{\alpha f_0 R}{2}, \quad x \geq 0, \tag{12}$$

where u_1 is the absolute velocity along the outer edge.

Since our present analysis is inviscid, the condition of a continuous velocity across the streamline separating the upstream incoming and the downstream outgoing currents does

not have to be satisfied. We do satisfy, of course, the continuity of velocities along the streamlines passing through the cross-section connecting the currents and the BE ($x=0$),

$$\overline{v_\theta}\,|_{x=0} = u\,|_{x=0}\,. \tag{13}$$

And, we also satisfy conservation of the Bernoulli integral along the wall,

$$u\,|_{y=0} = -u_1, \quad x \geq 0. \tag{14}$$

For simplicity, we shall suppose that the velocity in the incoming and retroflected currents depends linearly on y, allowing the above-mentioned velocity jump along the separating streamline ($y=-d_1$).

Although a velocity jump across a streamline is in general allowed (in analogy to the slip condition), we introduce the initial conditions in a manner that allows continuous velocities. To do so, we assume that, initially, when the BE starts to develop, a complete retroflection occurs, so that $Q=q$ and $d_1=d_2$. To satisfy Eq. (13), we take $R=d_1$ and $u\,|_{y=-d_1}=0$ at $t=0$. Furthermore, the growth of the BE in time implies $R>\max(d_1, d_2)$; and, therefore, from Eq. (13) we deduce for the incoming current in the region $x\geq 0$,

$$u = -\frac{u_1\,(R - d_1)}{R} \quad at\ y = -d_1, \tag{15a}$$

and, for the retroflected current,

$$u = \frac{u_1\,(R - d_2)}{R} \quad at\ y = -d_1. \tag{15b}$$

For the linear current velocity profiles, Eqs. (12)–(15) yield:

$$u = \frac{\alpha f_0}{2}(-y - R), \quad 0 \leq -y \leq d_1;$$
$$u = \frac{\alpha f_0}{2}\,(-y + R - d_1 - d_2), \quad d_1 < -y \leq d_1 + d_2. \tag{16}$$

Both currents are geostrophic so that,

$$\frac{\partial h}{\partial y} = -\frac{f}{g'}u(y) \approx \frac{f_0}{g'}u(y). \tag{17}$$

Integrating Eq. (17) with a substitution of Eq. (16), and taking into account that h should be continuous across the separating streamline between the incoming and retroflected currents ($y=-d_1$), we obtain:

$$h = -\frac{\alpha f_0^2}{4g'}y\,(2R + y) + h_0, \quad 0 < -y \leq d_1, \tag{18a}$$

and

$$h = \frac{\alpha f_0^2}{4g'}\,\{-y\,[2\,(d_1 + d_2 - R) + y] + 2d_1\,(2R - d_1 - d_2)\}$$
$$+ h_0, \quad d_1 < -y \leq d_1 + d_2. \tag{18b}$$

Next, we use the volume fluxes relationships,

$$Q = \int_0^{-d_1} hu\,dy, \quad q = -\int_{-d_1}^{-(d_1+d_2)} hu\,dy. \tag{19}$$

Substituting Eqs. (16) and (18) into Eq. (19), and solving the equations for d_1 and d_2, we finally have,

$$d_{1,2} = R - \delta_{1,2}, \tag{20}$$

where

$$\delta_1 = \left[R^2 - \frac{4g'}{\alpha f_0^2}\left(\tilde{h} - h_0\right)\right]^{1/2},$$

$$\delta_2 = \left[R^2 - \frac{4g'}{\alpha f_0^2}\left(\tilde{h} - H\right)\right]^{1/2}, \tag{21}$$

$$\tilde{h} = \left[h_0^2 + \frac{2f_0 Q}{g'}\right]^{1/2},$$

$$H = \left[h_0^2 + \frac{2f_0(Q - q)}{g'}\right]^{1/2} \tag{22}$$

Using Eqs. (18), (20), and (21), it is easy to show that $h=\tilde{h}$ at $y=-d_1$ and $h=H$ at $y=-(d_1+d_2)$, as should be the case. The solution will be completed in the next subsections.

3.3 The balance of forces in the $\gamma \to 0$ case

To obtain the expressions for F_1 and F_2, we substitute Eqs. (16), (18), and (20) to (22), into Eq. (11). After some algebra, we find,

$$F_1 = \frac{\alpha^3 f_0^4}{240g'}\left(2R^5 - 5\delta_1^3 R^2 + 3\delta_1^5\right) + \frac{\alpha^2 f_0^2 h_0}{12}\left(R^3 - \delta_1^3\right), \tag{23}$$

$$F_2 = \frac{\alpha^3 f_0^4}{240g'}\left[2R^5 - 5\left(\delta_1^2 - \delta_2^2\right)R^3 - 5\delta_2^3 R^2 + 5\delta_1^2\delta_2^3 - 2\delta_2^5\right]$$
$$+ \frac{\alpha^2 f_0^2 h_0}{12}\left(R^3 - \delta_2^3\right), \tag{24}$$

where Eqs. (21) and (22) have also been employed.

The leading-order expressions for F_3 and F_4 can be obtained by using the polar coordinate system (r, θ) with the basic equation,

$$\frac{\overline{v_\theta}^2}{r} + f\overline{v_\theta} = g'\frac{\partial h}{\partial r}, \tag{25}$$

where $\overline{v_\theta}$ is given by Eq. (1), and the boundary condition of continuous h is, $h=H$ at $r=R$. The approximate solution is:

$$h(r) = \frac{\alpha(2 - \alpha)f_0^2}{8g'}\left(R^2 - r^2\right) + H. \tag{26}$$

The volume of the circular eddy is $V = 2\pi \int_0^R h(r) r dr$, which together with Eq. (26) yields,

$$V = \pi R^2 \left[\frac{\alpha(2-\alpha) f_0^2 R^2}{16 g'} + H \right]. \tag{27}$$

Therefore, under assumption that $C_\eta = -dR/dt$ (i.e. the epicenter of BE moves out of the coast but this eddy itself touches the coastline),

$$F_3 = \pi R^2 f_0 \left[\frac{\alpha(2-\alpha) f_0^2 R^2}{16 g'} + H \right] \frac{dR}{dt}. \tag{28}$$

Defining F_4 in the same manner as in Nof (1981), we obtain from Eqs. (1) and (26) that

$$F_4 = 2\pi \beta \int_0^R r \, |\psi| \, dr,$$

where

$$\psi = \int_R^r \overline{v_\theta} h dr = \frac{\alpha f_0}{2} \int_R^r \left[\frac{\alpha(2-\alpha) f_0^2 \left(R^2 r - r^3 \right)}{8 g'} + r H \right] dr,$$

giving,

$$F_4 = \frac{\pi \alpha \beta f_0 R^4}{8} \left[\frac{\alpha(2-\alpha) f_0^2 R^2}{24 g'} + H \right]. \tag{29}$$

3.4 The general force balance in the $\gamma \neq 0$ case

Finally, Eq. (9) with Eqs. (23), (24), (28) and (29) gives a nonlinear equation for dR/dt,

$$\frac{(\alpha f_0)^3}{240} \left[2 \left(1 + \cos\gamma \right) R^5 - 5 \cos\gamma \left(\delta_1^2 - \delta_2^2 \right) \right.$$

$$R^3 - 5 \left(\delta_1^3 + \delta_2^3 \cos\gamma \right) R^2$$

$$+ \left(3\delta_1^5 + 5\delta_1^2 \delta_2^3 \cos\gamma - 2\delta_2^5 \cos\gamma \right) \right] + \frac{\alpha^2 f_0 g' h_0}{12}$$

$$\left[(1 + \cos\gamma) R^3 - \left(\delta_1^3 + \delta_2^3 \cos\gamma \right) \right] - \pi R^2$$

$$\left[g' H \left(\frac{dR}{dt} + \frac{\alpha \beta R^2}{8} \sin\gamma \right) + \frac{\alpha(2-\alpha) f_0^2 R^2}{16} \right.$$

$$\left. \left(\frac{dR}{dt} + \frac{\alpha \beta R^2}{12} \sin\gamma \right) \right] = 0. \tag{30}$$

Note that Eqs. (21) and (22) were also used in the derivation.

3.5 Combining the mass conservation into the momentum flux in the most general case $\gamma \geq 0$

To close the system of differential equations, we use the mass conservation equation. Substitution of Eqs. (27) and (22) into Eq. (10) yields:

$$Q - q = 2\pi R \left\{ \frac{\alpha(2-\alpha) f_0^2 R^2}{8 g'} + \left[h_0^2 + \frac{2 f_0 (Q-q)}{g'} \right]^{1/2} \right\}$$

$$\frac{dR}{dt} - \frac{\pi f R^2}{\left[(g' h_0)^2 + 2 f_0 g' (Q-q) \right]^{1/2}} \frac{dq}{dt}. \tag{31}$$

We note that, in the special case of a steadily retroflected current (i.e., $dq/dt = 0$), the second term disappears. As it turned out, this term is small and can be neglected even in the case of the unsteady retroflected current. Specifically, the numerical solution, which will be briefly described below, shows that the second term relative contribution is no more than $\sim O(0.01)$. With this neglect, we get a quadratic equation for $(Q-q)$ whose physically relevant solution $(Q \geq q)$ is,

$$Q - q = \frac{\mu}{g'} \left\{ \frac{\alpha(2-\alpha) f_0^2 R^2}{8} + f_0 \mu \right.$$

$$\left. + \left[(f_0 \mu)^2 + \frac{\alpha(2-\alpha) f_0^3 R^2 \mu}{4} + \left(g' h_0 \right)^2 \right]^{1/2} \right\}, \tag{32}$$

where $\mu = 2\pi R dR/dt$. At this point, substitution of the mass conservation Eq. (32) into the geostrophic and circular conditions Eqs. (21), (22), and the momentum (30) leads to our desired single differential equation (of the first order) for R as a function of t with the known parameters Q, h_0, g', f_0, α, β, and γ. This equation is extremely cumbersome (occupying more than a full page) and, therefore, is not presented here.

For the initial conditions at $t=0$, we take the initial radius R_i of the BE to coincide with the width of incoming current d_1. Therefore, it follows from Eq. (20) that $\delta_1 = 0$, and from Eq. (21) for δ_1 we conclude that

$$R_i = \frac{2}{f_0} \left[\frac{g' \left(\tilde{h} - h_0 \right)}{\alpha} \right]^{1/2}. \tag{33}$$

Our complete desired solution will be shortly presented. Before doing so, however, it is necessary to re-examine the scales in the initial conditions. This is done in the next subsection.

3.6 Examination of the instantaneous initial formation limit

Since the initial conditions involve the instantaneous creation of an eddy, it is not a priori obvious that our earlier short-and-long scales are valid at that time. We shall now show that
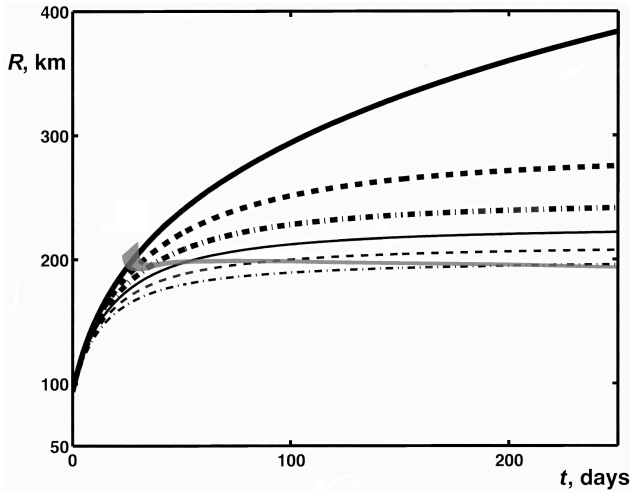
Fig. 4. The theoretically calculated zero PV BE radius versus time for $\gamma = 0^0$ (solid thick line), 15^0 (dashed thick line), 30^0 (dash-and-dotted thick line), 45^0 (solid thin line), 60^0 (dashed thin line), and 75^0 (dash-and-dotted thin line). The parameters are: $\alpha=1$, $h_0=0$, and $\beta=2.3\times10^{-11}$ m^{-1} s^{-1}. The solid line time-dependency is proportional to $t^{1/4}$. Note that the rings usually reach a *terminal* size. The shaded region was determined from the one-and-a half-layer model numerical experiments and denotes the time at which the eddies detach. This detachment issue is beyond the scope of this paper and will be addressed in a companion article.

this is, nevertheless, the case. To do so, we first note from Eq. (32) that,

$$\left| \frac{1}{f_0 R} \frac{dR}{dt} \right| < \frac{4g'Q}{\pi\alpha(2-\alpha)f_0^3 R^4}, \tag{34}$$

and, second, we note that, for $h_0=0$ and $t=0$, Eq. (33) takes the form:

$$R_i = \frac{2}{f_0} \left[\frac{\left(2f_0 g'Q\right)^{1/2}}{\alpha} \right]^{1/2}, \tag{35}$$

where, as before, the subscript "i" indicates the initial conditions.

Substituting Eq. (35) into the right-hand side of Eq. (34) leads to:

$$\left| \frac{1}{f_0 R} \frac{dR}{dt} \right| < \frac{\alpha}{8\pi(2-\alpha)}, \tag{36}$$

which is valid at the initial time. We now further note that the right-hand side of Eq. (36) is maximal for $\alpha=1$ (i.e., zero PV; here we recall that α cannot exceed unity because the PV of the eddies cannot be negative), so that,

$$\left| \frac{1}{f_0 R} \frac{dR}{dt} \right| < \frac{1}{8\pi} \approx 0.04,$$

implying that, even at the beginning of the BE development, the scale dR/dt is much smaller than the scale $f_0 R$.
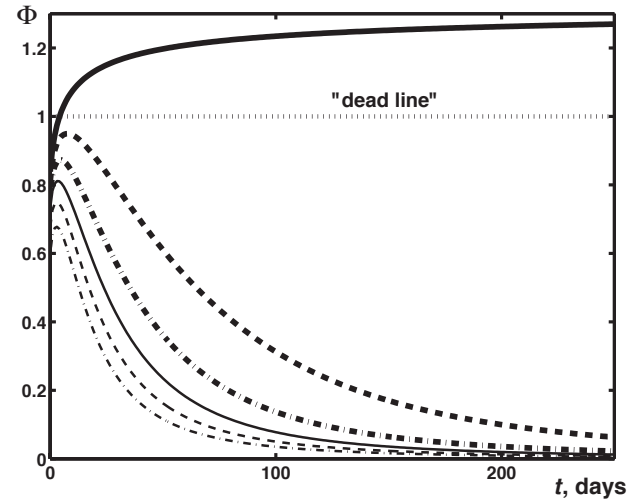

Fig. 5. The same as in Fig. 4, but for volume flux partition Φ. The dotted "dead line" shows the limit of physical relevance ($q=0$, $\Phi=1$). The physically impossible positioning of the solid line (no slant case) *above* this line corresponds to the "vorticity paradox". That impossible positioning disappears even for a small slant of $15°$ (dashed line).

4   Numerical solution of the ODE system

We solved the system Eqs. (30), (32), which is subject to the initial condition (33) by using the Runge-Kutta method of the fourth order. We used the following parametric values: $Q=70$ Sv; $g'=2\times10^{-2}$ ms^{-2}; $f_0=8.8\times10^{-5}$ s^{-1} (corresponding to 35^0 of latitude). We took the values zero and 300 m for h_0, and the values 2.3×10^{-11} and 6×10^{-11} m^{-1} s^{-1} for β. The values of α and γ were varied between 0.1 and 1.0, and between zero degrees and 89^0, respectively. For the case of zero PV and zero near-shore thickness, the evolution the BE radius with time is shown in Fig. 4. Here, the theoretical evolution at infinity is not very far from the value at $t=250$ days. It is seen that, although the radius increases monotonically for any value of γ, its growth for nonzero γ quickly becomes very slow, and there exist asymptotic values of R that decrease with growing γ. Physically, these asymptotes correspond to the balance between the combined effect of F_1 and F_2, and the β – force, F_4. The analogous picture for $h_0=300$ m is similar, but the asymptotical values are somewhat smaller. The maximal difference is for $\gamma=75^0$ for which we obtain an asymptotical value of 181 km instead of 195 km.

Once the growth of the BE diminishes, only a very small part of the incoming mass flux goes into the BE. This is shown in Fig. 5, which displays Φ as a function of time for $\alpha=1$, $h_0=0$. It is seen that, only when the wall is zonal ($\gamma=0$), Φ increases monotonically. The corresponding curve intersects the "dead line" curve $\Phi=1$, indicating that the vorticity paradox occurs in the area above this line. Finally,

Φ approaches an asymptotic value, which is close to 4/3. When $\gamma \neq 0$, the graphs quickly reach their maximal values, which decrease with growing γ, and then go down and approach zero. Increasing h_0 leads to a slight increase in the peaks. We see that for $\gamma \geq 15^0$, Φ does not reach unity regardless of the value of α. Note that for $\alpha=1$ and $h_0=0$, the maximal values of Φ can be expressed approximately as $1.012+0.32 \exp(-\gamma/3.41)-\gamma/225$. For $h_0=300$ m, they are larger, but not much larger. The maximal difference is when $\gamma=75^0$ for which the peak value of Φ is 0.78 instead of 0.68.

Figure 6 shows the influence of varying PV on the evolution of BE radius (Fig. 6a) and Φ (Fig. 6b) for $\gamma=30^0$ and $h_0=0$. The graphs become smoother with decreasing α. According to Eq. (32), the initial radius of the BE grows, and so our system gradually approaches the condition of balance between the currents momentum-flux and the BE β-force. Therefore, as α decreases, the growth of the BE over time becomes weaker and more uniform, and so does the required mass flux. We note that, starting from $\gamma=45^0$, our model does not work for very large PV (with $\alpha \approx 0.1$) because, in that case, the β-force exceeds the combined effect of the currents already at the initial moment of time. So, by analogy with the situation described by Nof (1999), the BE should leak as a result of being forced by β into the wall. We expect that, under such conditions, the BE cannot be nearly circular.

Qualitatively similar results were obtained for the magnified value of β. However, as expected, the asymptotical values of R and maximal values of Φ for $\gamma \neq 0$ were reduced. For example, in the case $\alpha=1.0$, $h_0=0$, $\beta=6 \times 10^{-11}$ m^{-1} s^{-1}, we obtained the asymptotical values of R to be approximately 230, 200, 185, 170, and 160 km, and maximal values of Φ to be 0.84, 0.73, 0.63, 0.54, and 0.44 for γ being 15^0, 30^0, 45^0, 60^0, and 75^0, respectively.

5 Numerical simulations using a one-and-a-half layer model

5.1 Numerical model description

We used a modifed version of the Bleck and Boudra (1986) reduced gravity isopycnic model with a passive lower layer, and employed the Orlanski (1976) second-order radiation conditions for the open boundary. The downstream streamlines were not disturbed when they crossed the boundary, suggesting that these open boundary conditions are satisfactory. In addition, changing the location of the boundary did not alter the behavior of the interior flow, which indicated that the boundary conditions are sufficient.

We chose the initial PV so that the starting value of α was 0.1, 0.4, and 1.0. The basin size was 3200×1600 km, and the continent was modeled by one fixed meridional wall (600 km long), and one adjacent wall that could be either zonal (2200 km long) or inclined by the angle γ; in this connection, γ varied between 15^0 and 75^0 with a step of 15^0.
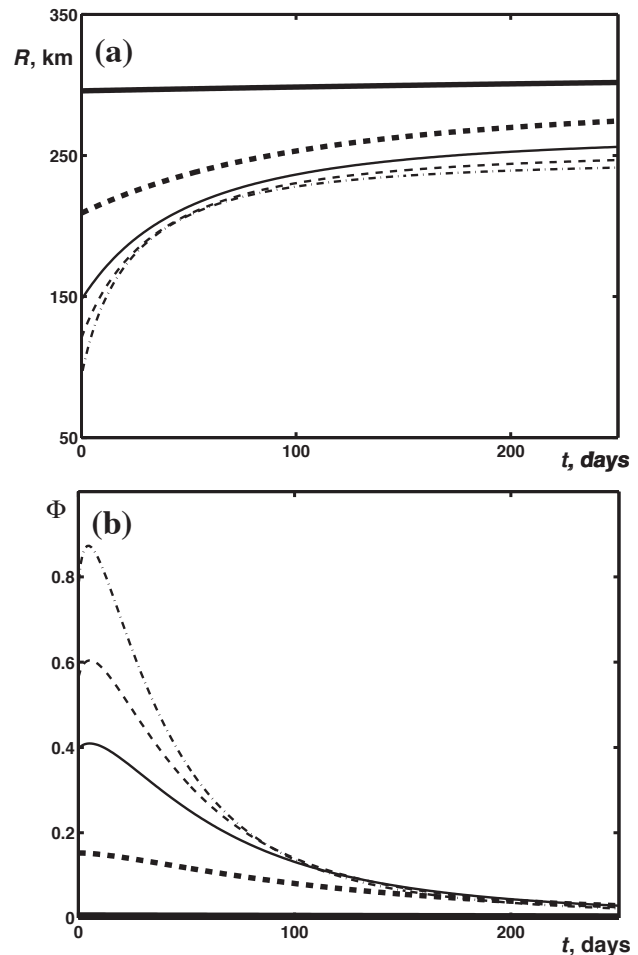

Fig. 6. Theoretical plots of the BE radius (a) and Φ (b) versus time for $\alpha=0.1$ (solid thick lines), 0.2 (dashed thick lines), 0.4 (solid thin lines), 0.6 (dashed thin lines), and 1.0 (dash-and-dotted thin lines). Parameters values: $\gamma=30^0$, $h_0=0$, $\beta=2.3 \times 10^{-11}$ m^{-1} s^{-1}. Note that the line for $\alpha=0.1$ in Fig. 6b practically coincides with the abscissa.

The walls were assumed to be slippery. The experiments began by turning on the flow at $t=0$; the numerical source was an open channel containing streamlines that were parallel to the wall for the incoming current, and zonal for the outgoing flow. As in our theoretical model, the initial velocity profile across the channel was linear, and the depth profile was parabolic. The numerical parameters of the model were: a time step of 120 s, a grid step of 20 km, and a Laplacian viscosity coefficient of $\nu=700$ m^2 s^{-1} for $\gamma>15^0$, 1000 m^2 s^{-1} for $\gamma=15^0$, and 1800 m^2 s^{-1} for the zonal wall. The high value in the last case was the lowest we could choose for stability. The reduced gravity was $g'=2 \times 10^{-2}$ ms^{-2}, the Coriolis parameter $f_0=8.8 \times 10^{-5}$ s^{-1}, and the prescribed flow $Q=70$ Sv. We took β to be 2.3×10^{-11} m^{-1} s^{-1} (realistic) and 6×10^{-11} m^{-1} s^{-1} (magnified), and the initial depth of the upper density layer at the wall to be zero and 300 m.
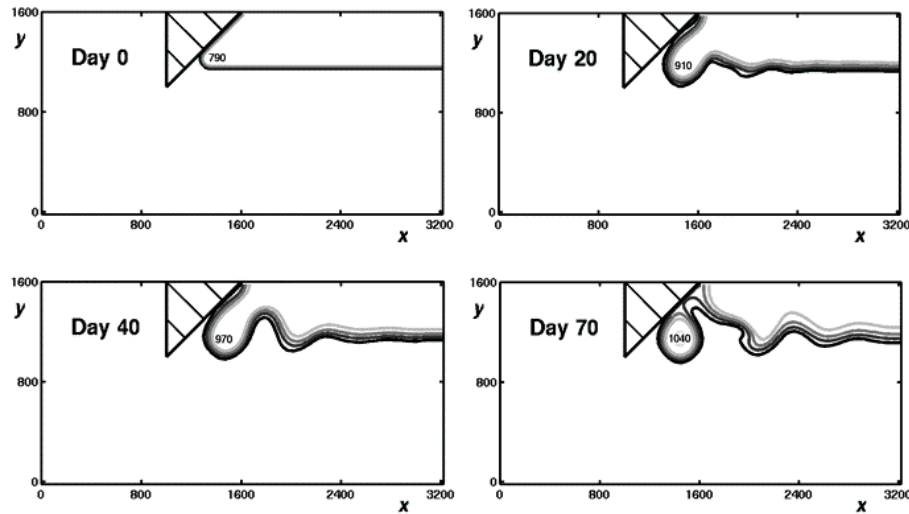
Fig. 7. Typical numerical experiment showing the growth of the BE. Note that the retroflected current is one-dimensional downstream. Spacing between contours represents increments of 200 m and the maximum thickness at the center of the BE is given within the eddy. Parameter values: $h_0=0$, $\alpha_{\text{init}}=1.0$, $\gamma=45^0$, $\beta=6\times10^{-11}\,\text{m}^{-1}\,\text{s}^{-1}$.

The modeled time in all our experiments was long, about 210 days. The above choices for resolution were adequate for our characteristic Rossby radius of 30 km, which corresponded to $H\approx350$ m with our choice of g' and f_0. Furthermore, these choices always allowed for at least nine grid points across the downstream current, which is also adequate.

Several comments should be made at this point. First, in all our comparisons, we used the *magnified* value of β in order to make the development of BE faster and less sensitive to the distorting effect of viscosity. Second, as in NP, the frictional forces altered the PV, and, consequently, the value of α decreased during the experiments. To make the parameters of our model and numerics closer to each other, we estimated the value of α after each 10 days of simulated time and reintroduced this value into our theoretical model. For a coastal slant of 60^0 and more, the decrease in α led to a squeezing of the BE into the wall, so that our model did not allow the calculation of $R(t)$ and $\Phi(t)$ for some of the time intervals. Instead of this, we artificially interpolated these functions, supposing $R(t)$ to be *nearly constant*, and assuming *negative* values of $\Phi(t)$. Alternatively, we performed the theoretical calculations with using a constant value of α, which was obtained by averaging over the full time of the BE development.

Third, the values of $\Phi(t)$ in the numerical simulations, which were calculated with a period of 1 day, were subject to strong local oscillations with periods of about 5 days, so we used the polynomial fitting to smooth these oscillations out. In addition, although we calculated Q and q numerically through the ending grid points of cross-sections (which were chosen to be close to the lines of given depth of the upper layer) we could not determine Φ accurately. This is because the error inherent in the choice between two neigh-

boring points could be as high as 0.15. Otherwise, we estimated the values of $R(t)$ based on the simulations obtained every 10 days, and, consequently, the results for R look much more stable than those for Φ.

5.2 Results

Thickness contours of a typical numerical simulation are shown in Fig. 7. We see that the BE gradually develops in time without altering the one-dimensionality of the downstream retroflected flow. Figure 8a, b and c shows a comparison of the radius of the BE during the development time for $\gamma=0^0$, $\gamma=30^0$, and $\gamma=60^0$ all with $h_0=0$. The starting value of α was 1. The results of our analytical model are given for α which was altered in time (solid curves) and averaged over the period of BE development (dashed curves). For every ten days, solid circles indicate the numerical values. The analytical results are in satisfactory agreement with the numerics, especially for $\gamma=0^0$. With increasing γ, the agreement becomes a little worse, indicating that, as a result of growing coastal slant, the radius decreases more slowly in the numerics than in our model. Nevertheless, our comparison is adequate.

The comparison of Φ, which is in general satisfactory, is given in Fig. 9. Here, the open circles show the fitted numerical values. At times, the results of our model and the numerical simulations differ significantly at the beginning of development (of the first BE), when the numerically obtained value of Φ can even be negative (Fig. 9b). As Fig. 9a illustrates, however, this is not always the case. Often the results agree from the beginning of the experiment. The former issue might be an outcome of our numerical initialization. Later in the BE development, the agreement improves in
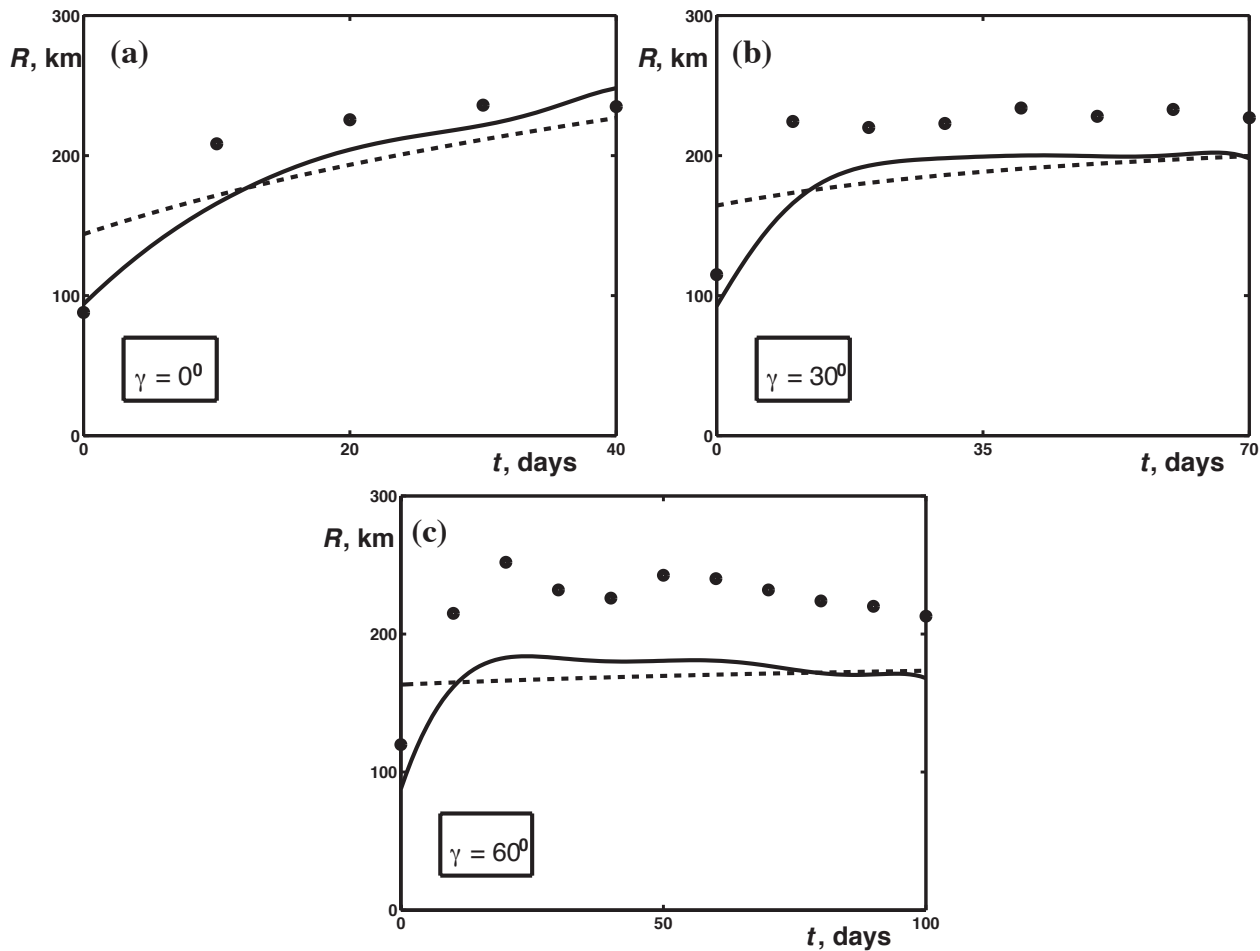
Fig. 8. The modeled and numerical values of the BE radius during the development for $h_0=0$ and three different slants (0^0, 30^0, and 60^0). All runs started with zero PV ($\alpha=1$). However, since numerical friction alters the PV, the theoretical computations were continuously adjusted on the basis of either a gradual numerically-altered value of α (solid curves) or an averaged value (dashed curves). As before, the numerical values (solid circles) are given every 10 days. For the solid line the initial value of α was unity whereas the final value was 0.224 **(a)**, 0.317 **(b)** and 0.444 **(c)**. The dashed line is based on averages, 0.423 (a), and 0.326 (both b and c). We note that, in the case (c), the final value of α got larger than average value because of decreasing R.

general, although in the case of zonal coastline (Fig. 9a), the theoretically obtained curve for averaged α agrees with the numerical simulations worse than that for altered αu The numerics in Fig. 9c do show some oscillations around the small theoretical values. This might be an effect of a meandering outgoing current in the numerical experiments. In addition, we note that when the theoretical value of $\Phi=(Q-q)/Q$ is small, its relative error could be large because it incorporates errors in Q and q when $q\approx Q$. It should be also noted that, in some of our runs, which started with $\alpha=0.4$ (not shown), the numerical value of Φ noticeably increased at the end of the numerical simulation, which is probably an effect of the incipient development of the next eddy.

6 Summary and conclusions

We developed a nonlinear analytical model of the BE formation and growth (Fig. 2), taking into account a nonzero thickness of the upper layer around the retroflection (H) and a slant of the coastline (γ). The main results can be summarized as follows:

1. The BE grows approximately as $t^{1/4}$ only in the case of a *zonal* coastline (i.e., no slant). When the slant is *nonzero*, the growth rate slows down and almost completely diminishes as the slant increases (Fig. 4). This leads to a terminal radius, which corresponds to the situation where the northeastward component of the northward β-force exactly balances the southwestward momentum-flux of the incoming and outgoing currents. The northeastward component of the Coriolis force is
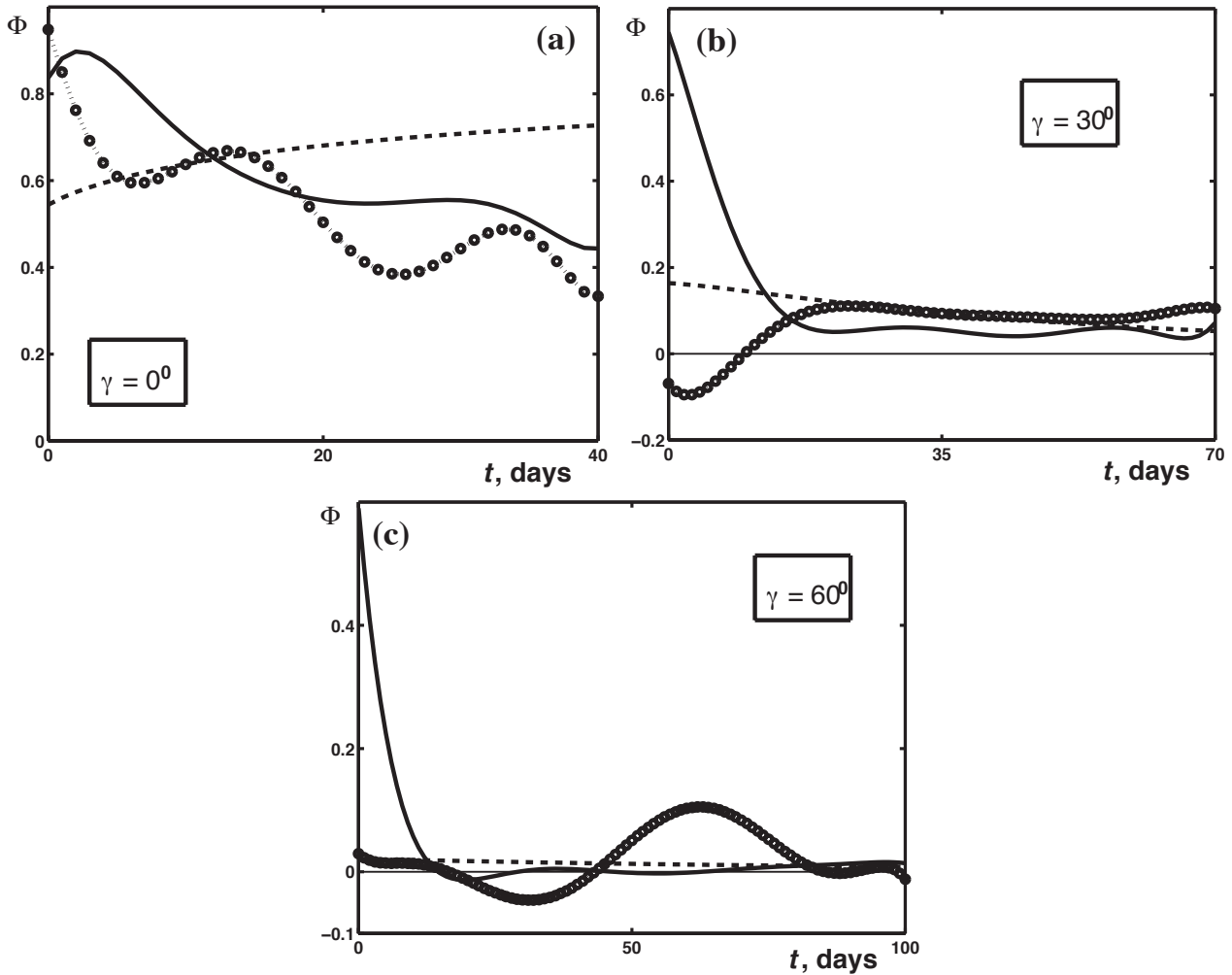
Fig. 9. The same as Fig. 8, but for modeled (solid and dashed line) and numerical (overlapping open circles) values of the volume flux partition Φ.

zero in this terminal case because the eddy is not growing so that it is not forced off the wall.

2. When the slant is not zero, the mass flux going into the BE is not constant. At first, it grows fast and achieves a peak value; then it decreases and tends to zero (Fig. 5).

3. When the slant of the coastline exceeds 15^0, the theoretical peak of the mass flux going into the BE with zero PV is smaller than the value of incoming flux implying the disappearance of the "vorticity paradox".

The above theoretical results are all in satisfactory agreement with the one-and-a half-layer numerical simulations (Figs. 6, 7, 8 and 9). As the growth of the BE is limited by an asymptotic value, the final radius of detached ring is expected to decrease with a growing slant. For example, in the zero PV and vanishing thickness along the wall case (i.e., $\alpha=1$ and $h_0=0$), the radii cannot exceed 220 km for $\gamma=45^0$

and 195 km for $\gamma=75^0$. We note that, using the simple time-averaged retroflection model from a *zonal* coastline model, Pichevin et al. (1999) found the theoretical radii of Agulhas eddies to be 227 km, which is somewhat smaller than our value for $\gamma=15^0$ (about 279 km) and $\gamma=30^0$ (about 242 km). However, this could be because the authors obtained the radii at the moment of detachment, not the asymptotic values for infinite time.

In our calculation, the mass partition Φ is time-dependent but the process is time-averaged and this gives less than a unity for Φ when the angle γ is larger than 15^0. This means that we have circumvented the vorticity paradox issue for slanted coastlines but the question of what happens when there is a small slant or no-slant remains open. Another remaining issue is that of the rings shedding process – this is beyond the scope of this paper and will be addressed in a companion article.

Like many other retroflection solutions, our solution has its counter-intuitive aspects. First, because the BE is anti-cyclonic, our solution exists only for those incoming currents whose upstream vorticity is anticyclonic. The solution breaks down for currents whose vorticity is cyclonic and the issue is reconciled by accepting the essential role of viscosity in altering the vorticity to the required downstream structure within the BE. That alteration of vorticity probably takes place in the ocean even in the anticyclonic case where we expect α to gradually decrease with time. Without such a decrease, the upstream speeds (though not the transports) must constantly increase as the BE grows. This accommodates for the increasing velocity along the eddy edge, which, via Bernoulli, is transmitted both upstream and downstream. Second, with the exception of the zero PV case, which we discuss in detail, it is hard to conceive of a uniform PV retroflection. This is why we simply assumed a linear velocity structure upstream and within the eddy. Our numerical simulations suggest that, because we used integrated techniques involving momentum fluxes, the detailed velocity distribution is smoothed out anyway so that it makes very little difference what profile one chooses.

Appendix A

List of symbols

AC	Agulhas Current
BE	basic eddy
C_x	eddy migration rate in the zonal direction
C_y	eddy migration rate in the meridional direction
$C_\xi C_\eta$	eddy migration rates in the rotated coordinate system
d_1	width of incoming current
d_2	width of retroflected current
F_1	force of incoming current
F_2	force of retroflected current in projection to ξ-axis
F_3	Coriolis force associated with the migration of the eddy
$F_4\beta$	force of the eddy
f	the Coriolis parameter
f_0	approximate absolute value of the Coriolis parameter at the eddy center
g'	reduced gravity
h	upper layer thickness
H	upper layer thickness outside the retroflection area
h_0	upper layer thickness at the wall
$\widetilde{h}$	upper layer thickness in the stagnant wedge situated between the incoming and retroflected currents
$\overline{h}$	undisturbed upper layer thickness
MOC	meridional overturning circulation
NP	Nof and Pichevin (2001)
PV	potential vorticity
Q	mass flux of the incoming current
q	mass flux of the retroflected current
R	radius of the eddy (a function of time)
R_d	Rossby radius of the eddy (a function of time)
R_f	radius of the eddy at the moment of detachment
R_i	initial radius of the eddy
r	radius in polar coordinate system
s	area of integration
Sv	Sverdrup (10^6 m^3 s^{-1})
t	time
$\hat{t}$	time in the fixed coordinate system
u, v	velocities in the zonal and meridional directions
$u^* v^*$	velocities in the rotated coordinate system
$\boldsymbol{u}^*$	vector with coordinates $u^* v^*$
u_1	absolute value of the current velocity at the edge
V	volume of the eddy
$\overline{v_\theta}$	orbital speed

x, y zonal and meridional coordinate axes in the moving system
$\hat{x}, \hat{y}$ zonal and meridional coordinate axes in the fixed system
α vorticity (twice the Rossby number)
γ slant of coastline
$\delta_1 \delta_2$ differences between the eddy radius and current widths d_1, d_2, respectively
$\Delta\rho$ difference between densities of lower and upper layer
ε small parameter defined as $\beta R_d / f_0$
θ angle in polar coordinate system
μ parameter defined as $2\pi R d R / dt$
$\xi\eta$ axes of rotated moving coordinate system
$\hat{\xi}, \hat{\eta}$ axes of rotated fixed coordinate system
ρ upper layer density
Φ ratio of mass flux going into the eddies and incoming mass flux
ϕ path of integration
ψ streamfunction

References

Arruda, W. Z., Nof, D., and O'Brien, J. J.: Does the Ulleung eddy owe its existence to β and nonlinearities?, Deep-Sea Res., 51, 2073–2090, 2004.

Bleck, R. and Boudra, D.: Wind-driven spin-up in eddy resolving ocean models formulated in isopycnic and isobaric coordinates, J. Geophys. Res., 91, 7611–7621, 1986.

Boudra, D. B. and Chassignet, E. P.: Dynamics of the Agulhas retroflection and ring formation in a numerical model, I. The vorticity balance, J. Phys. Oceanogr., 18, 280–303, 1988.

Chassignet, E. P. and Boudra, D. B.: Dynamics of the Agulhas retroflection and ring formation in a numerical model, II. Energetics and ring formation, J. Phys. Oceanogr., 18, 304–319, 1988.

de Ruijter, W. P. M.: Asymptotic analysis of the Agulhas and Brazil Current systems, J. Phys. Oceanogr., 12, 361–373, 1982.

de Ruijter, W. P. M., Biastoch, A., Drijfhout, S. S., Lutjeharms, J. R. E., Matano, R. P., Pichevin, T., van Leeuwen, P. J., and Weijer, W: Indian-Atlantic interocean exchange: Dynamics, estimation and impact, J. Geophys. Res., 104, 20 885–20 910, 1999.

Gordon, A. L., Lutjeharms, J. R. E., and Gründlingh, M. L.: Stratification and circulation at the Agulhas Retroflection, Deep-Sea Res., 34, 565–599, 1987.

Gordon, A. L. and Haxby, W. F.: Agulhas eddies invade the South Atlantic: Evidence from Geosat altimeter and shipboard conductivity-temperature-depth survey, J. Geophys. Res., 95, 3117–3127, 1990.

Lutjeharms, J. R. E.: The Agulhas Current, Springer-Verlag, Berlin-Heidelberg-New York, XIV, p. 330, 2006.

Nof, D.: On the β-induced movement of isolated baroclinic eddies, J. Phys. Oceanogr., 11, 1662–1672, 1981.

Nof, D.: Strange encounters of eddies with walls, J. Mar. Res., 57, 1–24, 1999.

Nof, D.: The momentum imbalance paradox revisited, J. Phys. Oceanogr., 35, 1928–1939, 2005.

Nof, D. and Pichevin, T.: The retroflection paradox, J. Phys. Oceanogr., 26, 2344–2358, 1996.

Nof, D. and Pichevin, T.: The establishment of the Tsugaru and the Alboran gyres, J. Phys. Oceanogr., 29, 39–54, 1999.

Nof, D. and Pichevin, T.: The ballooning of outflows, J. Phys. Oceanogr., 31, 3045–3058, 2001.

Orlanski, I.: A simple boundary condition for unbounded hyperbolic flows, J. Comput. Phys., 21, 251–269, 1976.

Ou, H. W. and de Ruijter, W. P. M.: Separation of an internal boundary current from a curved coast line, J. Phys. Oceanogr., 16, 280–289, 1986.

Pichevin, T., Nof, D., and Lutjeharms, J. R. E.: Why are there Agulhas Rings?, J. Phys. Oceanogr., 29, 693–707, 1999.

van Aken, H. M., van Veldhoven, A. K., Veth, C., de Ruijter, W. P. M., van Leeuwen, P. J., Drijfhout, S. S., Whittle, C. P., and Rouault, M.: Observations of a young Agulhas ring, Astrid, during MARE in March 2000, Deep-Sea Res., 50, 167–195, 2003.

Weijer, W., de Ruijter, W. P. M., Dijkstra, H. A., and van Leeuwen, P. J.: Impact of interbasin exchange on the Atlantic Overturning Circulation, J. Phys. Oceanogr., 29, 2266–2284, 1999.